ACS APPLIED MATERIALS & INTERFACES
Research Article
Cite This: ACS Appl. Mater. Interfaces 2017, 9, 35651-35663
www.acsami.org

cRGD/TAT Dual-Ligand Reversibly Cross-Linked Micelles Loaded with Docetaxel Penetrate Deeply into Tumor Tissue and Show High Antitumor Efficacy in Vivo

Yaqin Zhu,[†,‡] Jian Zhang,[†] Fenghua Meng,[†] Chao Deng,[†] Ru Cheng,[†] Jan Feijen,*[,†,‡] and Zhiyuan Zhong*[,†]

[†]Biomedical Polymers Laboratory, and Jiangsu Key Laboratory of Advanced Functional Polymer Design and Application, College of Chemistry, Chemical Engineering and Materials Science, Soochow University, Suzhou 215123, P. R. China

[‡]Department of Polymer Chemistry and Biomaterials, Faculty of Science and Technology, MIRA Institute for Biomedical Technology and Technical Medicine, University of Twente, P.O. Box 217, 7500 AE Enschede, The Netherlands

Supporting Information

ABSTRACT: The application of cell-penetrating peptides like TAT for in vivo targeted delivery is limited because the penetration behavior is not cell-specific. Herein, we designed cRGD and TAT comodified cross-linkable micelles (cRGD/TAT CMs), in which the TAT peptide was shielded by relatively long poly(ethylene glycol) (PEG) chains. Docetaxel (DTX)-loaded cRGD/TAT CMs were very stable with minimal drug leakage under physiological conditions, whereas rapid DTX release took place in a reductive environment. Flow cytometry showed that the cRGD/TAT CMs with molar ratios of 20% cRGD and 10% TAT (cRGD20/TAT10 CMs) were selectively and efficiently taken up by $\alpha_v\beta_3$-overexpressing U87MG glioma cells, with 8.3-fold and 18.3-fold higher uptake than cRGD20 CMs and PEG CMs, respectively. DTX-loaded cRGD20/TAT10 CMs exhibited a high cytotoxicity in U87MG cells, leading to rapid apoptosis of the tumor cells. Uptake mechanism studies revealed that cRGD20/TAT10 CMs mainly employed the caveolae-mediated endocytotic pathway and efficiently escaped from the lysosomes. Notably, cRGD20/TAT10 CMs had a long circulating time of 6.25 h in vivo, due to cross-linking of the micelles and shielding of the TAT peptide. Moreover, DTX-loaded cRGD20/TAT10 CMs exhibited a significantly higher accumulation and deeper penetration in subcutaneous U87MG glioma tissue compared to cRGD20 CMs and PEG CMs, leading to superior antitumor efficacy in vivo. Therefore, this dual-ligand strategy provides an effective way to realize tumor-specific penetration and inhibition.

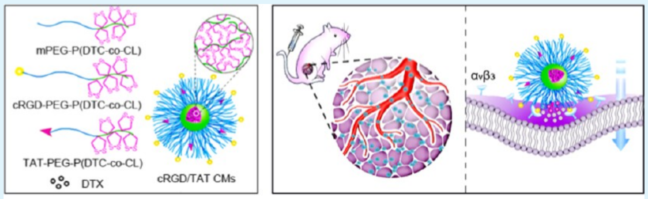

Self-assembly of cRGD/TAT reversibly crosslinked micelles

Deep tumor penetration, efficient cellular uptake by tumor cells and high antitumor efficacy

KEYWORDS: *Biodegradable micelles, reduction-sensitive, tumor penetration, anticancer drug, targeted delivery*

1. INTRODUCTION

Drug-loaded nanocarriers, such as liposomes, nanoparticles, and micelles, have shown distinct advantages over free therapeutic molecules, such as targeted delivery and reduction of side effects. However, their delivery efficiency was still hindered by several physiological barriers.[1−4] Among them, the cell membrane presents a significant barrier to nanocarriers as most of the drugs exert their pharmacologic action inside the cells.[5,6] To enhance the therapeutic effect of nanomedicines, various methods to improve the cellular uptake have been explored. The most frequently used method is to decorate the surface of the nanocarrier with targeting ligands (such as cRGD, transferrin, folate, and antibodies) based on the fact that specific receptors are overexpressed on many kinds of tumor cells.[7−11] Unfortunately, receptor-mediated endocytosis still has not led to satisfactory outcomes although higher cellular uptakes were observed in many studies. The discovery of cell-penetrating peptides (CPPs) opened the door for greatly enhanced cellular uptake of nanocarriers.[12] Among all of the CPPs, TAT peptide derived from the HIV TAT protein was mostly studied. TAT-based drug-delivery strategies have been applied in various in vitro studies, which all showed a considerable improvement in the cellular uptake of nanocarriers.[13−16] It seems that TAT peptide easily penetrates cell membrane barriers and therefore also can be used for nanocarrier delivery.[17] Xiong et al. designed RGD4C and TAT dual-functionalized DOX-loaded micelles, which readily delivered mdr1 siRNA into resistant MDA435/LCC6 cells, inducing improved P-gp silencing, enhanced DOX uptake, and cytotoxicity in vitro.[14] However, TAT has no selectivity to cells as the penetration of TAT mostly relies on the interaction of positively charged arginine residues within TAT and the negatively charged cell membrane.[18] This largely limited the in vivo application of TAT-based nanocarriers because it may also cause nonspecific penetration of normal cells. To avoid this drawback of the use of TAT peptide, some new strategies have

Received: August 18, 2017
Accepted: September 27, 2017
Published: September 27, 2017

DOI: 10.1021/acsami.7b12439
ACS Appl. Mater. Interfaces 2017, 9, 35651−35663

Scheme 1. Illustration of cRGD and TAT Cofunctionalized, Reduction-Responsive, and Reversibly Cross-Linked Biodegradable Micelles (cRGD/TAT CMs) for Targeted Subcutaneous Glioma Therapy in Vivo[a]

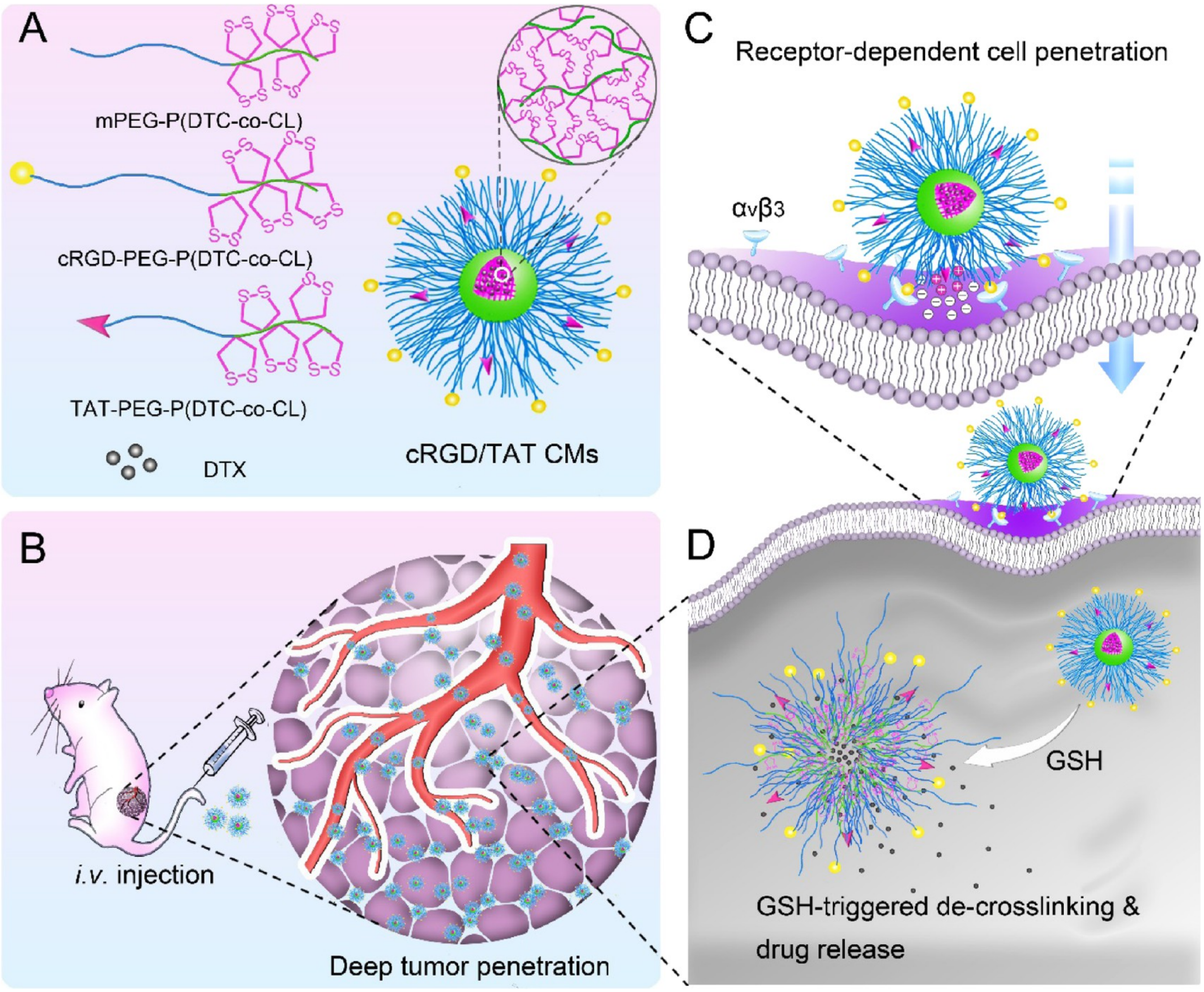

[a](A) The micelles were assembled from copolymers of mPEG$_{5k}$-P(DTC-*co*-CL), cRGD-PEG$_{6k}$-P(DTC-*co*-CL), and TAT-PEG$_{2k}$-P(DTC-*co*-CL); (B) Docetaxel (DTX)-loaded cRGD/TAT CMs actively target glioma and penetrate deep into tumor tissues; (C) DTX-loaded cRGD/TAT CMs exhibit efficient receptor-dependent cell penetration; (D) DTX is rapidly released into the cytoplasm via GSH-triggered de-cross-linking of cRGD/TAT CMs.

been developed. One approach is to hide TAT by the introduction of long poly(ethylene glycol) (PEG) chains containing stimuli-responsive bonds.[19−21] In another strategy, TAT peptide was blocked by electrostatic interaction with a protecting negatively charged compound.[22] The above strategies led to shielding of the positively charged TAT during circulation, whereas its penetration ability at the target site was selectively restored by either cleavage of the shielding PEG or removal of the electrostatic interaction with the protecting negatively charged compound in the tumor microenvironment. However, it is well known that the pH and concentration of enzymes in the tumor microenvironment vary in different types of tumors or in different regions of the tumor tissue,[23−25] which may affect the exposure of the protected TAT. Therefore, we followed a different approach without the use of stimuli-responsive bonds and negatively charged protecting compounds. TAT peptide was coupled to short PEG chains (M_n = 2k), which were shielded by long PEG molecules (M_n = 5k) to avoid nonspecific cell penetration and degradation by serum enzymes in the blood circulation. The targeting ligands cRGD peptide were attached to longer PEG (M_n = 6k) chains to allow full exposure. We hypothesized that when the micelles accumulated at the tumor site due to the EPR effect, bonding of cRGD to its receptors ($\alpha_v\beta_3$ integrins) will bring the TAT in close proximity of the cell membrane, allowing TAT to exert its penetration ability (Scheme 1).

In this approach, the stability of the nanocarrier in the circulation is a prerequisite to allow the ligands to exert their function at the tumor site. We have reported that using the proprietary functional monomer, dithiolane trimethylene carbonate (DTC), reversibly cross-linked polymersomes or micelles can be easily designed.[26,27] Compared to non-cross-linked nanocarriers, cross-linked nanocarriers exhibited longer circulation times in vivo.[28] After the micelles enter the cells, the disulfide bonds can be converted into thiol groups in the intracellular reductive environment, leading to micellar swelling and subsequent rapid drug release (Scheme 1). We expected to achieve maximal cytostatic effects in the tumor by combining the dual-ligand approach with reversibly cross-linked micelles.

In this study, the optimal density of TAT at the micellar surface was first screened by flow cytometry. The in vitro antitumor efficacy of DTX-loaded cRGD20/TAT10 CMs in $\alpha_v\beta_3$-overexpressing U87MG glioma cells was assessed by 3-(4,5-dimethylthiazol-2-yl)-2,5-diphenyltetrazolium bromide (MTT) and apoptosis assays. Subsequently, the uptake mechanism and lysosomal escape behavior were studied by flow cytometry and confocal microscopy measurements, respectively. The in vivo pharmacokinetics, imaging, biodistribution, and tumor penetration were also investigated. Finally, the in vivo antitumor efficacy of DTX-loaded cRGD20/TAT10 CMs was determined using an U87MG subcutaneous mice model.

2. MATERIALS AND METHODS

2.1. Materials. Dithiolane trimethylene carbonate (DTC) was synthesized as in our previous report.[29] Free DTX (10 mg/mL) was prepared by dissolving DTX in a 1:1 mixture of Tween 80 and absolute ethanol. Other materials used are described in the Supporting Information.

2.2. Cell Culture and Animal Studies. The murine fibroblast L929 cells and human glioma U87MG cell line were purchased from the cell institute of the Chinese Academy of Sciences (Shanghai, China). Cells were cultured as a monolayer at 37 °C in a humidified atmosphere containing 5% CO_2 in Dulbecco's modified Eagle's medium containing 1% (v/v) penicillin and streptomycin and 10% (v/v) fetal bovine serum (FBS) according to our earlier protocol.[8]

Female Balb/c nude mice and Balb/c mice of 4−6 weeks age were purchased from the Model Animal Research Center of Nanjing University (Nanjing, China) and Shanghai SLAC Laboratory Animal Co., Ltd. (Shanghai, China), respectively. Mice were housed under normal specific pathogen-free conditions. The protocols of all animal experiments were approved by the Animal Study Committee of Soochow University.

2.3. Synthesis of Polymers. mPEG$_{5k}$-P(DTC-*co*-CL) was synthesized by ring-opening polymerization of DTC and ε-CL in DCM at 30 °C using MeO-PEG$_{5k}$-OH as an initiator and DPP as a catalyst (for details, see supplementary data and Figure S2). Ligand-functionalized polymers cRGD-PEG$_{6k}$-P(DTC-*co*-CL) and TAT-PEG$_{2k}$-P(DTC-*co*-CL) were synthesized by conjugating cRGD-SH or TAT-SH to MAL-PEG$_{6k}$-P(DTC-*co*-CL) or MAL-PEG$_{2k}$-P(DTC-*co*-CL) polymers, respectively (for details, see supplementary data and Figures S2−S6). Cy5-labeled PEG$_{5k}$-P(DTC-*co*-CL) polymer was synthesized in three steps (for details, see supplementary data and Figure S2B).

2.4. Preparation and Characterization of Blank and DTX-Loaded cRGD/TAT CMs. cRGD/TAT CMs were prepared by injection of mPEG$_{5k}$-P(DTC-*co*-CL), cRGD-PEG$_{6k}$-P(DTC-*co*-CL), and TAT-PEG$_{2k}$-P(DTC-*co*-CL) block copolymers at different molar ratios (75/20/5, 72.5/20/7.5, 70/20/10, 65/20/15, and 60/20/20; total polymer weight: 1 mg) in dimethylformamide (DMF) (10 mg/mL) into 0.9 mL of phosphate buffer (PB, 5 mM, pH 7.4). After 2 h standing at room temperature, the homogeneous dispersion was incubated at 37 °C in a shaking bath (THZ-C, Taicang Instrument Factory, Jiangsu, China) at 200 rpm overnight, followed by extensive dialysis against PB (5 mM, pH 7.4) for 12 h at room temperature. Control groups consisting of the nontargeting micelles (PEG CMs), cRGD-functionalized micelles (cRGD CMs), and TAT-functionalized micelles with PEG shielding (PEG/TAT CMs) or without PEG shielding (TAT100 CMs) were prepared similarly. Cy5-labeled micelles were prepared by insertion of 10% (molar ratio) of Cy5-PEG$_{5k}$-P(DTC-*co*-CL) polymer. The cross-linking of the micelles was confirmed by determination of the disappearance of the UV absorbance of DTC at 330 nm.

DTX-loaded micelles were prepared by injecting a mixture of block copolymers (10 mg/mL in DMF) and DTX (10 mg/mL in DMF) into PB (5 mM, pH 7.4). The drug-loading content (DLC) and drug-loading efficiency (DLE) were determined by high-performance liquid chromatography (HPLC). Briefly, DTT (final concentration: 20 mM) was added to DTX-loaded micellar suspensions (1 mg/mL, 200 μL), and the resulting suspensions were incubated at 37 °C in the shaking bath at 200 rpm overnight to completely de-cross-link the micelles. After addition of acetonitrile (800 μL), the samples were incubated in the shaking bath for 2 h. The solution was filtered using a poly(vinylidene fluoride) microfiltration membrane (pore size: 450 nm, Millipore), and the DTX concentration was determined by HPLC (Agilent Technologies 1260 Infinity, mobile phase: a mixture of acetonitrile and water (v/v = 1/1) and UV detection at 227 nm). The following conditions were used: column, Sepax GP-C18 (150 mm × 4.6 mm, 5 μm); injection volume, 20 μL; flow rate, 1.0 mL/min; retention time, 8.3 min.

DLC and DLE were obtained using the following formulae

$$\text{DLC (wt\%)} = (\text{weight of loaded drug/total weight of polymer and loaded drug}) \times 100$$

$$\text{DLE (\%)} = (\text{weight of loaded drug/weight of drug in feed}) \times 100$$

2.5. Cellular Uptake of Micelles. To establish the optimal density of TAT peptide, the cellular uptake of Cy5-labeled cRGD/TAT CMs with a molar ratio of 20% cRGD and different molar ratios of TAT peptide (5, 7.5, 10, 15, and 20%) was studied by flow cytometry and confocal laser scanning microscopy. Details are described in the Supporting Information.

2.6. Uptake Mechanism. To confirm whether the cellular uptake of cRGD20/TAT10 CMs in U87MG cells is receptor-dependent, $\alpha_v\beta_3$-negative L929 cells were used as control.[30] Briefly, U87MG cells (5×10^5 cells/well) or L929 cells (3×10^5 cells/well) were seeded in six-well plates and cultured for 24 h. Cy5-labeled micelles (PEG CMs, PEG/TAT10 CMs, cRGD20 CMs, or cRGD20/TAT10 CMs) were added to the medium with a final micelle concentration of 100 μg/mL and incubated for 4 h. The cells were then washed with PBS and harvested for flow cytometry as described in the Supporting Information for the cellular uptake of micelles. To study the energy-dependent process, the cells were preincubated for 30 min either at 4 °C or in the presence of NaN_3 (10 mM) at 37 °C. Cy5-labeled micelles were added (final micelle concentration of 100 μg/mL) and incubated at 4 or 37 °C for another 1 h. Furthermore, the uptake pathway was studied by pretreating cells with different endocytic inhibitors (chlorpromazine: 10 μg/mL, amiloride hydrochloride: 1 mg/mL, β-CD: 1 mg/mL) or the competitive inhibitor (heparin sodium: 1 mg/mL) at 37 °C for 30 min. Subsequently, Cy5-labeled micelles were added and incubated at 37 °C for another 1 h at a final micelle concentration of 100 μg/mL. Cells treated with PBS at 37 °C were used as control group. Subsequently, the cells were washed and harvested for flow cytometry as described above. The lysosomal escape behavior of the different Cy5-labeled micelles was studied by confocal microscopy. Briefly, U87MG cells were seeded at a density of 2×10^4 cells/well on round glass coverslips in 24-well plates and cultured at 37 °C for 24 h. Cy5-labeled micelles were added and incubated for 4 h at a micelle concentration of 100 μg/mL. For one group, the culture medium was replaced with fresh medium and the cells were incubated for another 4 h. For the other group, the cells were washed with PBS after removal of the culture medium. Cells of both groups were then stained with LysoTracker Green (200 nM) for 1 h, washed with PBS, fixed using 4% paraformaldehyde, stained with 4′,6-diamidino-2-phenylindole (DAPI) for 8 min, washed again with PBS, and finally examined with CLSM.

2.7. Apoptosis. U87MG cells were seeded in six-well plates at a density of 3×10^5 cells/well and cultured for 24 h. DTX-loaded micelles or free DTX (final DTX concentration: 1 μg/mL) were added and incubated for 4 h. Then, the medium was replaced with fresh medium, and the cells were incubated for an additional 20 h. Apoptotic cells were detected by staining with an Annexin V and propidium

DOI: 10.1021/acsami.7b12439

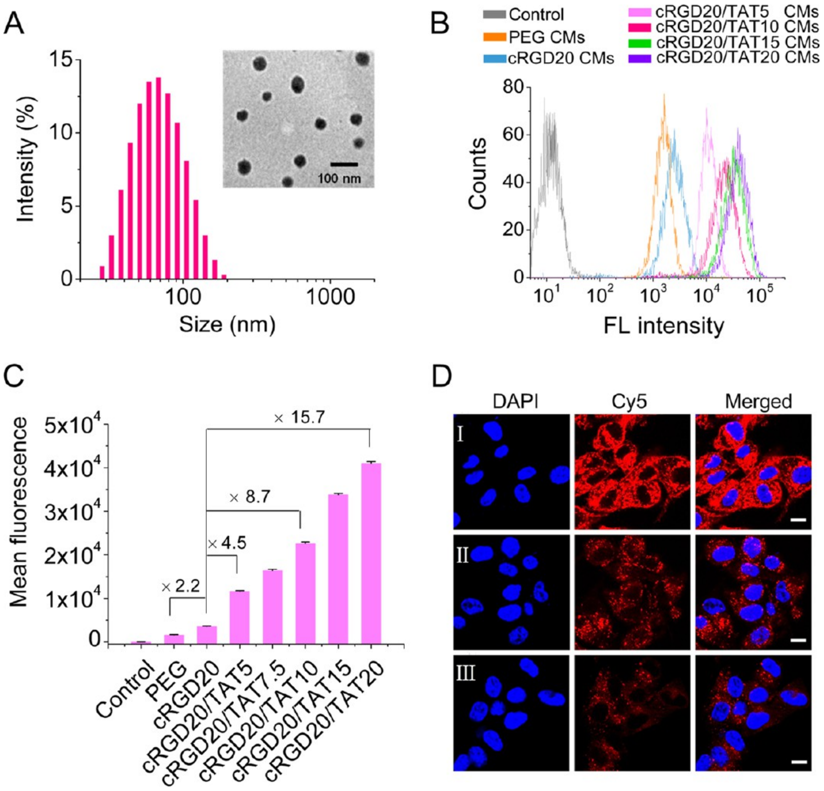

Figure 1. (A) Size distribution of blank cRGD20/TAT10 CMs determined by DLS and TEM. (B) Flow cytometry studies of U87MG cells after 4 h incubation with cRGD20/TAT CMs with different densities of TAT; cRGD20 CMs and PEG CMs were used as controls. (C) Quantitative analysis of fluorescence intensity of the above micelles; data are presented as average ± standard deviation ($n = 3$). (D) Confocal microscopy study of U87MG cells after 4 h incubation with cRGD20/TAT10 CMs (I); cRGD20 CMs (II); and PEG CMs (III), which were used as controls. The scale bar is 10 μm.

iodide kit (Sigma-Aldrich). Briefly, U87MG cells were detached with 0.25% trypsin (not containing ethylenediaminetetraacetic acid) and centrifuged at 156.5*g* for 5 min. The cells were washed twice with PBS and resuspended in 300 μL of binding buffer. After addition of Annexin V-FITC (5 μL) and propidium iodide (PI, 3 μL), the cell suspension was incubated at room temperature for 15 min in the dark. The cells were analyzed by flow cytometry within 1 h.

2.8. In Vivo Pharmacokinetics. Female Balb/c mice were used to investigate the in vivo pharmacokinetics of DTX-loaded micelles or free DTX. After tail vein injection of DTX-loaded micelles or free DTX (10 mg of DTX equiv/kg), ~50 μL of blood was taken from the retro-orbital sinus of Balb/c mice at different time points. Each blood sample was dissolved in lysis buffer (1% Triton X-100, 0.15 mL) with brief sonication. To extract DTX from blood, the samples were incubated with methanol (1 mL) at −20 °C overnight. After vortexing and centrifugation at 30 065*g* for 15 min, the DTX level of the supernatant was determined by HPLC. The elimination half-life ($t_{1/2\beta}$) of DTX in DTX-loaded micelles or free DTX was determined by fitting the experimental data using software Origin8 exponential decay 2 model: $y = A_1 \exp(-x/t_1) + A_2 \exp(-x/t_2) + y_0$, and taking $t_{1/2\beta} = 0.693 \times t_2$.

2.9. In Vivo Imaging. Subcutaneous U87MG tumor-bearing mice were obtained by transplanting tumor blocks (2−3 mm^3) into the right hind flank of the mice. When the average volume of the tumors reached a value of about 100 mm^3, 200 μL of Cy5-labeled micelles was injected into the tumor-bearing mice via the tail vein at a micelle dose of 20 mg/kg. At different time points (2, 6, 12, 24, and 48 h) post injection, the mice were anesthetized with pentobarbital sodium (10 mg/mL in PBS) at a dose of 62.5 mg/kg, and the distribution of the fluorescence in mice was determined using a near-infrared fluorescence imaging system (IVIS, Lumina II; Caliper, MA) with wavelength set at Ex = 633 nm and Em = 668 nm. At 48 h, the main organs and tumors were collected and their fluorescence images were acquired as described above.

2.10. Biodistribution. Quantitative analysis of the distribution of DTX-loaded micelles or free DTX in the tumor and in different organs was performed using U87MG tumor-bearing mice (three mice per group) following 12 h iv injection with DTX-loaded micelles or free DTX (10 mg DTX equiv/kg). The tumor, heart, liver, spleen, lung, and kidney were collected, washed with cold PBS, and weighed. To extract DTX, tissues were homogenized in 1 mL of methanol and the samples were incubated at −20 °C overnight. Supernatants were obtained after vortexing and centrifugation at 17 226*g* for 15 min and subsequently transferred to 1.5 mL centrifuge tubes. Methanol was removed by evaporation, and 750 μL of fresh methanol was added to each sample. After vortexing and centrifugation at 30 065*g* for 15 min, DTX levels were determined by HPLC as described above.

2.11. Tumor Penetration. The tumor penetration behavior of micelles was studied by immunofluorescent analysis. When the U87MG tumor reached a size of about 200 mm^3, Cy5-labeled micelles (micelle dose: 20 mg/kg) were injected into tumor-bearing mice via the tail vein. At 12 h post injection, U87MG tumors were harvested, fixed in 4% formalin overnight, embedded in paraffin, and sliced for immunofluorescence staining analysis according to our previous study[31] except that Alexa 488-conjugated donkey antirat secondary antibody was used in this study. Finally, the stained slices were studied with CLSM.

2.12. In Vivo Antitumor Efficacy. The therapeutic efficacy of DTX-loaded PEG CMs, cRGD20 CMs, cRGD20/TAT10 CMs, and free DTX was evaluated using subcutaneous U87MG glioma-bearing nude mice. Mice treated with PBS were used as control. When the tumor reached a volume of ~50 mm^3, the mice were randomly divided into five groups (six mice per group) and treated with the above formulations (10 mg DTX equiv/kg) via tail vein injection every 3 days for a total of four doses. Tumor growth was monitored, and

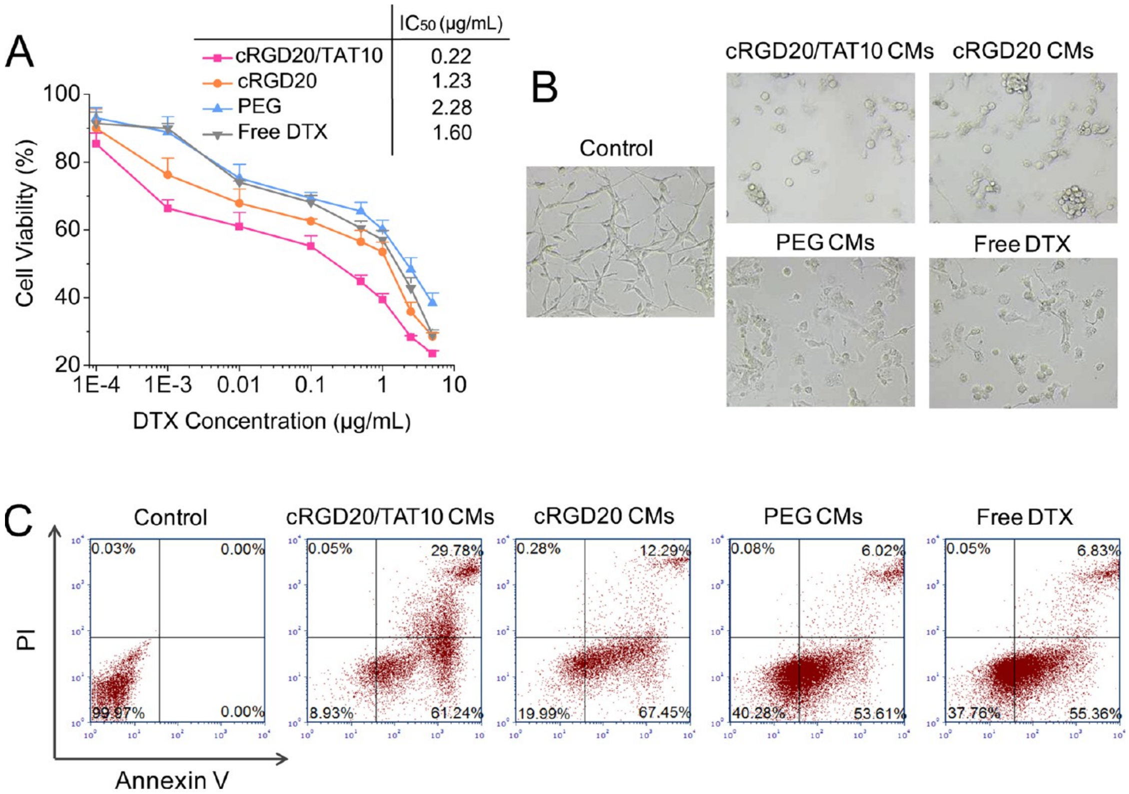

Figure 2. (A) U87MG cell viability after treatment with DTX-loaded micelles or free DTX at different DTX concentrations at 48 h (4 h treatment plus 44 h incubation with medium). (B) Change in morphology of U87MG treated as above at a DTX concentration of 1 μg/mL. (C) Apoptosis assay of U87MG cells after treatment with DTX-loaded micelles or free DTX at 24 h (4 h treatment plus 20 h incubation with medium) at a DTX concentration of 1 μg/mL.

tumor volume was measured by calipers and calculated according to the following formula: $V = 0.5 \times a \times b^2$, where a and b are the tumor dimensions at the longest and widest points of the tumor, respectively. At the experimental end point, the tumor, liver, heart, spleen, lung, and kidney were collected from one mouse of each group for histological analysis after staining with hematoxylin and eosin (H&E). In addition, to investigate the apoptosis of tumor cells induced by DTX, tumor tissues were further stained with terminal deoxynucleotidyl transferase dUTP nick end labeling (TUNEL) and finally evaluated with a digital microscope (Leica QWin, Germany). For quantitative analysis of TUNEL staining positive cells, the integral optical density (IOD) was measured by Image-Pro Plus 6.0 software (Media Cybernetics Inc., Newburyport, MA).

2.13. Statistical Analysis. All data are presented as mean ± standard deviation (SD). The statistical significance among groups was analyzed using one-way analysis of variance (ANOVA), after which post hoc tests with the Bonferroni correction were used for comparison between individual groups. P values <0.05 indicate statistical significance; $^{*}p < 0.05$, $^{**}p < 0.01$, $^{***}p < 0.001$.

3. RESULTS AND DISCUSSION

3.1. Stability, Reduction-Triggered Destabilization, and Drug Release from cRGD20/TAT10 CMs. A series of micelles was prepared with similar size distribution, as shown in Table S1. Typically, cRGD20/TAT10 CMs had an average size of 61 nm as determined by dynamic light scattering (DLS, Malvern Instruments, U.K.) with a uniform distribution as also shown by transmission electron microscopy (TEM) measurements (Figure 1A). It was noticed that the ζ potential of cRGD20/TAT10 CMs was negative, indicating that the positive charge of TAT peptide was successfully shielded by the long PEG chains. UV spectra showed that the characteristic absorbance of polymers at 330 nm, which originates from the dithiolane rings of DTC, completely disappeared in micellar dispersions (Figure S7A), indicating that the dithiolane rings in the micellar core spontaneously formed linear chains containing disulfide bonds via ring-opening polymerization.[29] The cross-linked micelles exhibited excellent colloidal stability against high-fold dilution (Figure S7B) or 10% FBS (Figure S7C). However, the size of TAT100 CMs quickly increased probably because the positively charged surface easily adsorbed negatively charged proteins present in the serum, resulting in micelle aggregation. In the presence of 10 mM GSH, which mimics the intracellular reductive environment, cRGD20/TAT10 CMs rapidly swelled to hundreds of nanometers (Figure S7D) probably because the hydrophilic/hydrophobic balance of the micelles had been destroyed due to the reduction of the disulfide bonds to thiol groups by GSH. Additionally, drug release from the micelles was studied in the presence or absence of 10 mM GSH (Figure S8). A drug-loading content (DLC) of 6.9 wt % was obtained at a theoretical DLC of 15 wt % for DTX-loaded cRGD20/TAT10 CMs (Table S2). Under physiological conditions, only 12.7% of the loaded drug was released from cRGD20/TAT10 CMs at 24 h, demonstrating that the cross-linked core effectively hindered drug leakage. In contrast, in the presence of GSH (10 mM), the drug release rate increased, with 54.1% release of drug in 8 h and 85.0% in 24 h, indicating that the drug can be rapidly released from the micelles in the intracellular reductive environment.

3.2. Establishing the Optimal Density of TAT Peptide in cRGD/TAT CMs. Previous studies have demonstrated that the cellular uptake of TAT-modified nanocarriers was closely related to the surface concentration of TAT peptide.[16,32]

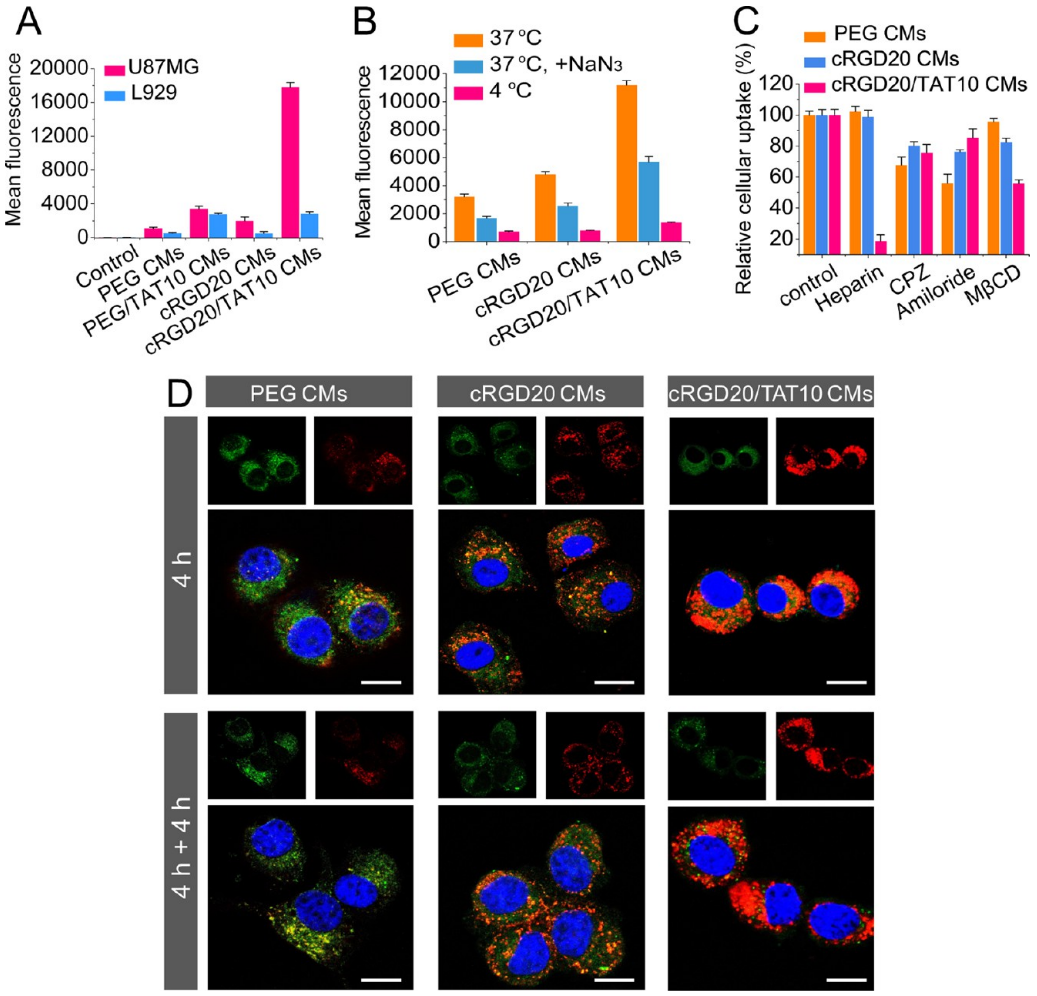

Figure 3. Uptake mechanisms of cRGD20/TAT10 CMs studied by flow cytometry and confocal microscopy. (A) Cellular uptake of different Cy5-labeled micelles in both $\alpha_v\beta_3$-overexpressing U87MG cells and $\alpha_v\beta_3$-negative L929 cells following 4 h incubation; cells without treatment were used as controls. (B) Cellular uptake of different Cy5-labeled micelles in the presence of ATPase inhibitor NaN_3 or at 4 °C following 1 h incubation; cells incubated with micelles under normal conditions were used as controls. (C) Relative cellular uptake of different Cy5-labeled micelles in the presence of the competitive inhibitor heparin or various endocytic inhibitors; cells incubated with micelles under normal conditions were used as controls. (D) Lysosomal escape behavior of Cy5-labeled cRGD20/TAT10 CMs observed by confocal microscopy after 4 h treatment with micelles or after 4 h treatment with micelles, followed by 4 h treatment with culture medium; Cy5-labeled PEG CMs and cRGD20 CMs were used as controls. Lysosomes were stained with LysoTracker Green (green), Cy5-labeled micelles were colored red, and cell nuclei were stained with DAPI (blue). The scale bar is 10 μm.

However, a high surface density of TAT peptide may result in instability of nanocarriers in the blood circulation and toxicity to normal cells.[33] Therefore, a proper density of TAT peptide is critical for the function of nanocarriers. Here, we prepared a series of Cy5-labeled cRGD/TAT CMs with different densities of TAT peptide (molar ratios: 5, 10, 15, 20%) and investigated the cellular uptake by flow cytometry. The density of cRGD was fixed at 20% (molar ratio) according to our previous study, in which PEG−SS−PCL micelles with similar size (61 ± 1 nm) and 20% (molar ratio) of cRGD exhibited efficient U87MG cell targeting.[8] Figure 1B,C shows that compared to nontargeted Cy5-labeled PEG CMs, cRGD20 CMs exhibited a 2.2-fold higher cellular uptake due to receptor-mediated endocytosis. Surprisingly, insertion of TAT into the cRGD20 CMs dramatically increased the cellular uptake (the cellular uptake of cRGD20/TAT10 CMs and cRGD20/TAT20 CMs increased by 8.7-fold and 15.7-fold, respectively, compared to that of cRGD20 CMs), further indicating that the cellular uptake of the micelles increased with increased surface concentration of TAT. However, we noticed that the ζ potential of the micelles also tends to become positive with increasing TAT density (Table S1), which may exert toxicity to cells. Therefore, an MTT assay was conducted to assess the cytotoxicity of cRGD/TAT CMs. Figure S9 reveals that 15% TAT in the micelles decreased the cell viability to about 91.8%, and the cells became partially shrunken as observed by microscopy (data not shown). Thus, considering these effects and the cytotoxicity, we selected 10% TAT peptide as the optimal density. Subsequently, the cellular uptake of Cy5-labeled cRGD20/TAT10 CMs was further studied by confocal microscopy. As shown in Figure 1D, cRGD20/TAT10 CM-treated cells displayed the strongest fluorescence intensity compared to those treated with Cy5-labeled cRGD20 CMs or PEG CMs, confirming the high cell penetration ability of cRGD20/TAT10 CMs.

3.3. In Vitro Cytotoxicity Assay.

The MTT assay was performed to assess the cytotoxicity of DTX-loaded micelles and free DTX for U87MG cells. As shown in Figure 2A, cRGD20/TAT10 CMs exhibited the highest cytotoxicity with the IC_{50} value of 0.22 μg/mL, which was 5.6-fold, 10.4-fold, and 7.3-fold lower than that of DTX-loaded cRGD20 CMs (1.23 μg/mL), PEG CMs (2.28 μg/mL), and free DTX (1.60 μg/mL), respectively, probably due to efficient cellular uptake and subsequent fast drug release as demonstrated above. The morphology of the U87MG cells after 48 h at a DTX concentration of 1 μg/mL was also studied (Figure 2B). Compared to the PBS group, DTX-loaded micelles or free DTX induced morphological changes of U87MG cells on different levels, among which cRGD20/TAT10 CM-treated cells exhibited a significant shrinkage with obvious reduction of pseudopodia. It has been reported that the invasion ability of U87MG cells decreases with decreasing pseudopodia formation.[34] Therefore, cRGD20/TAT10 CMs may exhibit the most strongest inhibition effect on U87MG cell invasion. To further investigate the apoptosis of U87MG cells induced by DTX, AnnexinV-FITC/PI was used for double staining of cells. The lower left, lower right, upper right, and upper left quadrants in the flow cytometry quadrant diagram indicated viable, early apoptotic, late apoptotic, and necrotic cells, respectively (Figure 2C). The percentage of total apoptotic cells after treatment with DTX-loaded cRGD20 CMs (79.74%) was much higher than that treated with DTX-loaded PEG CMs (59.63%) and free DTX (62.19%), indicating the important role of active targeting in tumor cell inhibition. Importantly, the DTX-loaded cRGD20/TAT10 CM-treated group induced the highest percentage of total apoptotic cells (91.02%), which was consistent with the MTT assay. It was also noticed that the early apoptotic cell population after treatment with DTX-loaded cRGD20/TAT10 CMs (61.24%) was similar to that after treatment with DTX-loaded cRGD20 CMs (67.45%), whereas a greater late apoptotic population was observed (29.78 vs 12.29%) probably because part of early apoptotic cells in the cRGD20/TAT10 CM-treated group had entered into the late stage of apoptosis, indicating that the efficient uptake of cRGD20/TAT10 CMs led to more and rapid apoptosis of tumor cells.

3.4. Uptake Mechanism of cRGD20/TAT10 CMs. To get more insight into the mechanism of action of cRGD20/TAT10 CMs, we further studied the uptake mechanism. First, to investigate whether the uptake of cRGD20/TAT10 CMs was receptor-dependent, nontargeted PEG/TAT10 CMs and $\alpha_v\beta_3$-negative fibroblast L929 cells were used as control group. Figure 3A shows that in U87MG cells the cellular uptake of cRGD20/TAT10 CMs was 6.3-fold higher than that of PEG/TAT10 CMs, whereas in L929 cells, there was no significant difference in the uptake between cRGD20/TAT10 CMs and PEG/TAT10 CMs, demonstrating that the endocytosis of cRGD20/TAT10 CMs is receptor-dependent. It was noted that in both cells, PEG/TAT10 CMs, compared to PEG CMs, exhibited higher cellular uptake probably because the introduction of TAT enhanced the ζ potential of PEG micelles (Table S1), resulting in stronger adsorption onto the cell membrane. Next, to reveal whether the uptake of cRGD20/TAT10 CMs was energy-dependent, cellular uptake in the presence of the ATPase inhibitor NaN_3 or at low temperature (4 °C) was investigated. Figure 3B reveals that both NaN_3 and low temperature significantly decreased the cellular uptake of micelles, indicating that the uptake of the micelles, including cRGD20/TAT10 CMs, is an energy-dependent process. This result was in line with previous studies, which also demonstrated that TAT-mediated endocytosis is energy-dependent.[18,35,36] At 4 °C, the cellular uptake of the micelles decreased substantially compared to that in the presence of NaN_3 at 37 °C. This was probably due to an increase of the viscosity of the cell culture medium and cell membrane rigidity with decreasing temperature, reducing the amount of micelles that effectively interacted with the cells.[37]

Before endocytosis, cell-penetrating peptides (CPPs) first electrostatically interact with extracellular anionic molecules, such as heparin sulfate proteoglycans (HSPGs), which are abundant on cell membranes.[38,39] To define the role of HSPGs in the cellular uptake of cRGD20/TAT10 CMs, heparin, an HSPG analogue, was used here to compete with the HSPGs at the cell surface. As shown in Figure 3C, heparin strongly inhibited the cellular uptake of cRGD20/TAT10 CMs by U87MG cells to 18.8% probably because the presence of heparin hindered the interaction of TAT peptide with the negatively charged HSPGs. This result again confirmed that electrostatic interactions with HSPGs on the cell membrane surface played a key role in exerting the cell penetration ability of TAT.

Then, the uptake pathways of cRGD20/TAT10 CMs in U87MG cells were studied. In general, the uptake pathways involve four basic mechanisms: macropinocytosis, clathrin-mediated endocytosis, caveolae-mediated endocytosis, and clathrin- and caveolae-independent endocytosis.[40] Here, the transport pathways of different micelles were explored by treating cells with different endocytic inhibitors at a concentration which is nontoxic to U87MG cells (Figure S10). Chlorpromazine (CPZ) specifically blocks clathrin-mediated endocytosis by preventing clathrin polymerization and obstructing the internalization mediated by clathrin-coated vesicles (CCVs).[41] As shown in Figure 3C, CPZ treatment decreased the cellular uptake of cRGD20/TAT10 CMs to 75.8%, similar to that of PEG CMs (77.7%) and cRGD20 CMs (80.3%), indicating that the clathrin-mediated pathway played a similar role in the internalization of the three different micelles. However, it was noticed that in the presence of amiloride hydrochloride, a specific macropinocytosis inhibitor,[42] the uptake was significantly decreased to 56.1% for PEG CMs, whereas less impact was found in the uptake of cRGD20 CMs (decreased to 76.3%) and cRGD20/TAT10 CMs (decreased to 85.4%), suggesting that macropinocytosis played a more important role in the uptake of nontargeted PEG CMs. Interestingly, an opposite tendency in the cellular uptake of different micelles was observed with the treatment of MβCD, an inhibitor for caveolae-mediated endocytosis.[43] MβCD had no influence on the uptake of PEG CMs, whereas it decreased the cellular uptake of cRGD20 CMs to 82.5%, indicating that caveolae-mediated endocytosis was involved in the cRGD20 CM uptake. For cRGD20/TAT10 CMs, a significant inhibition of cellular uptake (44.1%) was noticed, suggesting that caveolae-mediated endocytosis may be a major pathway for the internalization of cRGD20/TAT10 CMs by U87MG cells.

Different uptake pathways may lead to different intracellular fates. It was reported that cargos internalized by cells via the clathrin-mediated pathway and macropinocytosis were directed to the lysosomes, whereas cargos internalized via caveolae could bypass the lysosomal pathway.[40,44] Moreover, the intracellular fate may be different for different nanocarriers even with the same uptake pathways. Therefore, studying the colocalization of micelles with lysosomes and whether they have a subsequent escape mechanism may help us to further understand their mechanisms of action. As shown in Figure 3D, Cy5-labeled

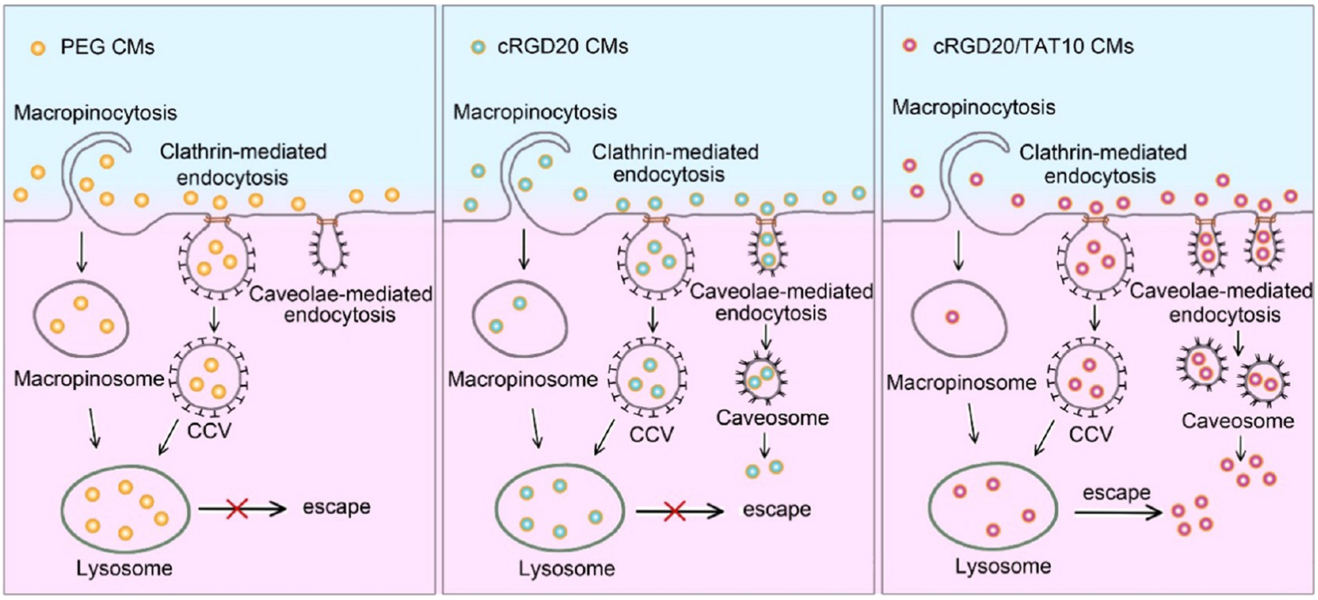

Figure 4. Schematic illustration of uptake pathways and lysosomal escape behavior of different micelles in U87MG cells.

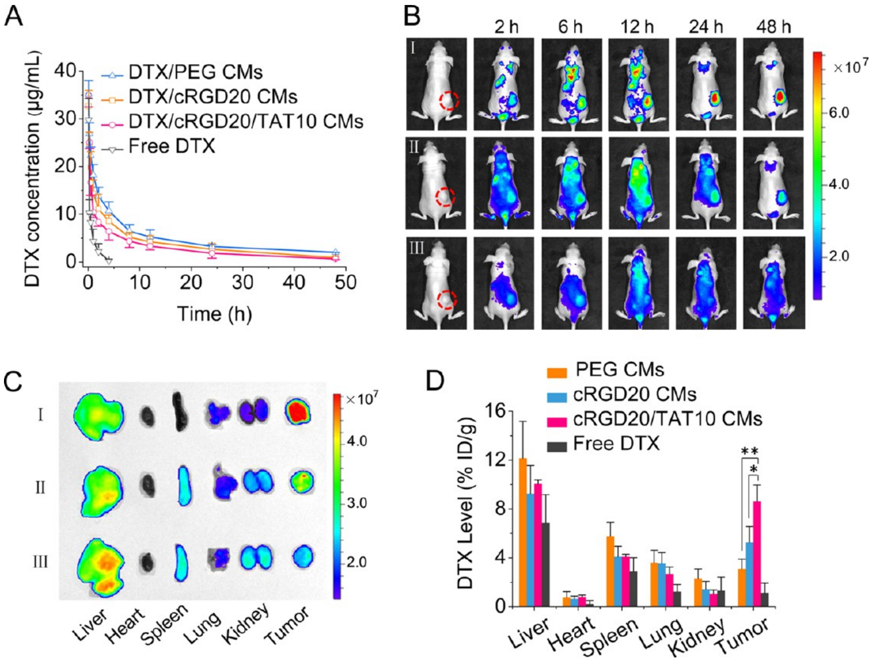

Figure 5. (A) In vivo pharmacokinetics of different DTX-loaded micelles and free DTX in Balb/C mice. (B) Targeted delivery of Cy5-labeled cRGD20/TAT10 CMs (I), cRGD20 CMs (II), and PEG CMs (III) in subcutaneous U87MG glioma-bearing mice. The red perforated circled areas indicate the location of the tumor. (C) Ex vivo images of main organs and tumors from mice treated with cRGD20/TAT10 CMs (I), cRGD20 CMs (II), and PEG CMs (III) at 48 h. (D) Biodistribution of different DTX-loaded micelles and free DTX in main organs and tumors 12 h after injection of DTX-loaded micelles at a DTX dose of 10 mg/kg. Data are presented as average ± standard deviation ($n = 3$). $*p < 0.05$, $**p < 0.01$.

PEG CMs were almost all colocalized with lysosomes, presenting a yellow appearance. After another 4 h incubation with fresh culture medium, PEG CMs were still entrapped in the lysosomes. In contrast, for the cRGD20 CMs, some of the red dots were separated from lysosomes probably because these micelles were endocytosed via caveolae and bypassed the endosomal/lysosomal pathway. However, similar to the uptake of PEG CMs, no more cRGD20 CMs escaped from lysosomes after another 4 h incubation, suggesting that when these micelles had entered the lysosomes they can hardly escape. Surprisingly, only a small fraction of cRGD20/TAT10 CMs was located in the lysosomes after 4 h incubation, and almost all of these micelles escaped from the lysosomes after another 4 h incubation, implying that in addition to the fraction of micelles bypassing the endosomal/lysosomal pathway the remaining part of cRGD20/TAT10 CMs could still efficiently escape from the lysosomes. It has been reported that among other factors the decreased pH in endosomes facilitates a membrane perturbation by TAT and subsequent TAT-modified cargo release into the cytoplasm.[18] On the basis of the results, possible uptake pathways and subsequent intracellular trafficking of different micelles in U87MG cells are illustrated in Figure

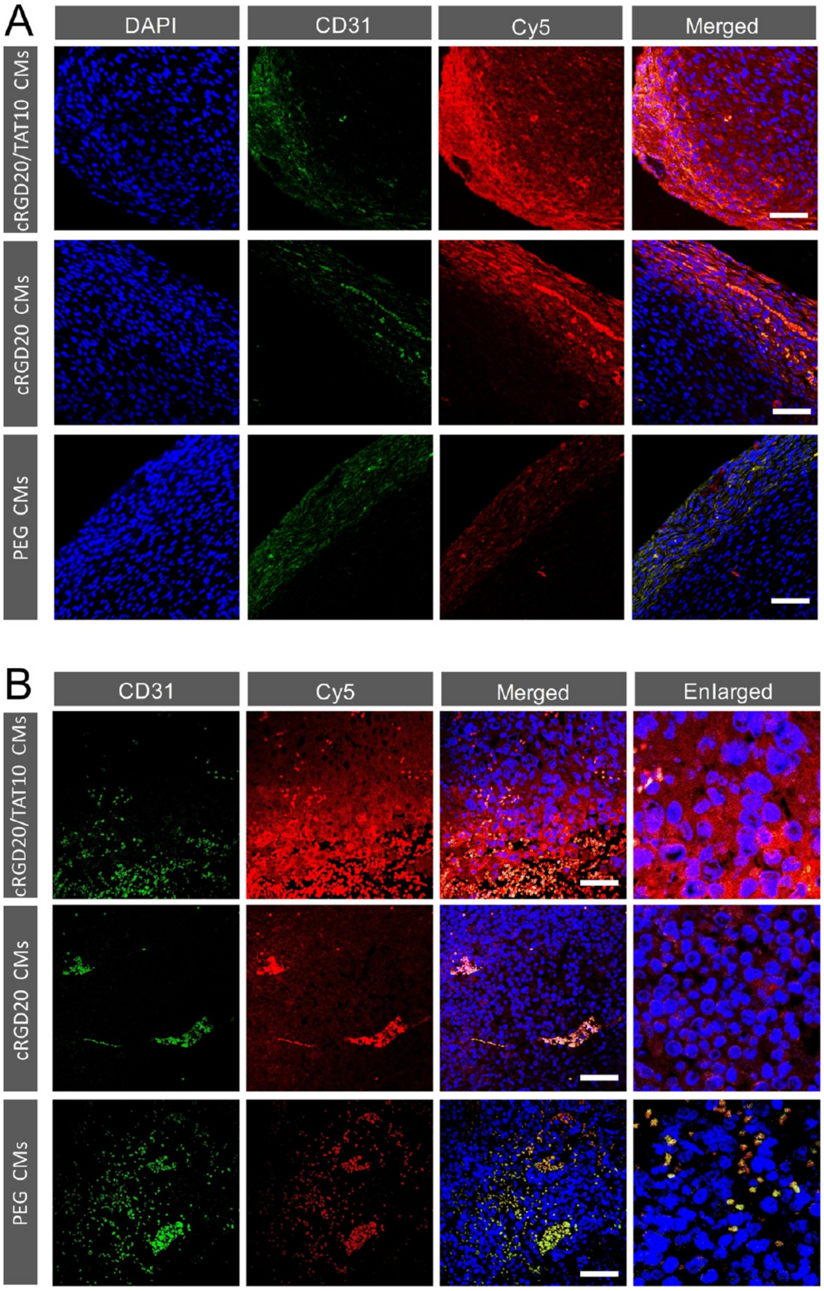

Figure 6. Tumor penetration behavior of Cy5-labeled cRGD20/TAT10 CMs studied by confocal microscopy. Penetration of Cy5-labeled micelles (A) at the edge and (B) at the interior of the tumor tissue. Tumor sections were obtained from U87MG tumor-bearing mice 12 h after tail vein injection of Cy5-labeled micelles. The nuclei are stained with DAPI (blue), blood vessels are stained with CD31 (green), and Cy5-labeled micelles are presented in red. The scale bar is 50 μm.

4, revealing that more cRGD20/TAT10 CMs entered the cytoplasm in time compared to PEG CMs and cRGD20 CMs. Consequently, also more cRGD20/TAT10 CMs were effectively de-cross-linked than the other micelles because GSH is mainly present in the cytoplasm.[45]

3.5. In Vivo Imaging, Pharmacokinetics, and Biodistribution.

In vivo stability is an important issue for realizing the tumor accumulation of nanocarriers.[28,46] Therefore, the in vivo pharmacokinetics of DTX-loaded cross-linked micelles were evaluated. As shown in Figure 5A, DTX-loaded cRGD20/TAT10 CMs had a prolonged elimination half-life ($t_{1/2\beta}$) of 6.25 h, which is comparable to that of DTX/cRGD20 CMs (6.47 h) or DTX/PEG CMs (6.62 h), indicating that the positively charged TAT peptide was well shielded by the long PEG layer. Notably, free DTX was rapidly cleared from the systemic circulation with an extremely short $t_{1/2\beta}$ of 0.72 h.[47,48] Moreover, it was noticed that the half-life of these cross-linked micelles was obviously longer than that of non-cross-linked micelle systems, as the premature disintegration of the cross-linked micelles in the systemic circulation was obviously prevented.[28] This also made the cross-linked micelles more suitable for systemic administration.

Noninvasive fluorescence imaging technology with Cy5-labeled micelles was utilized to monitor the real-time distribution and tumor accumulation of different micelles in a subcutaneous U87MG glioma-bearing nude mice model (Figure 5B). Exploiting the EPR effect, the three kinds of micelles can all accumulate at the tumor site due to their small

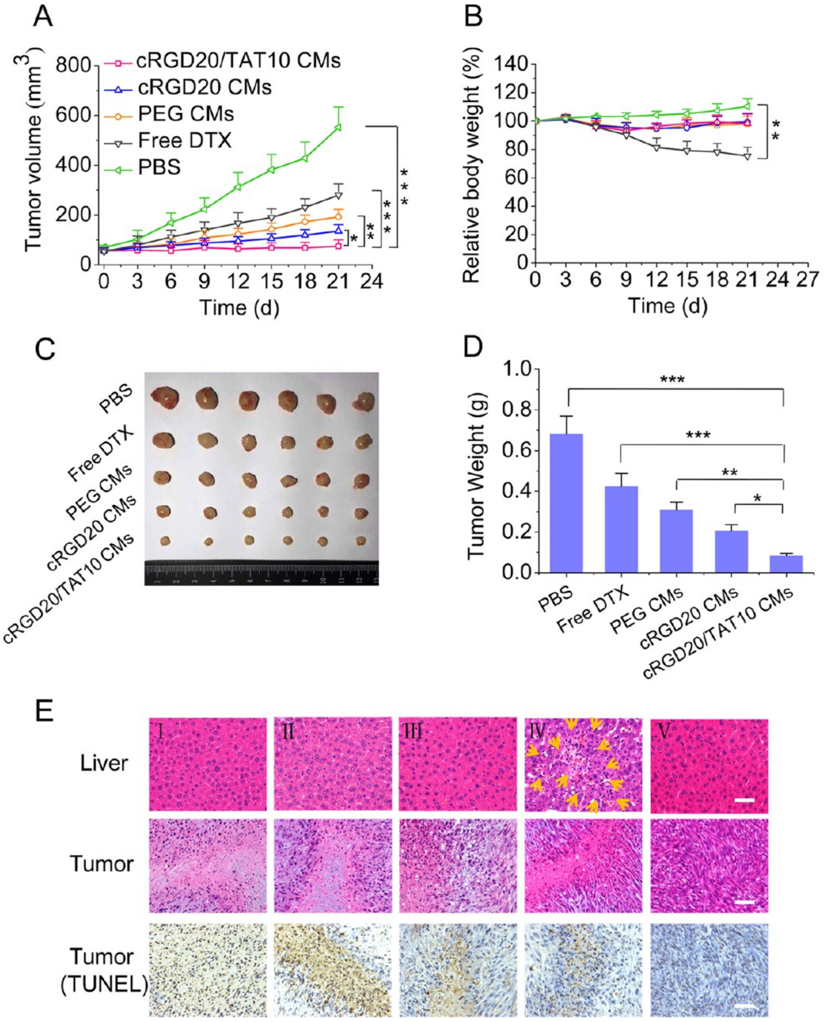

Figure 7. In vivo antitumor efficacy of different DTX-loaded micelles in subcutaneous U87MG glioma-bearing nude mice. (A) Tumor volume changes in time of mice treated with different DTX-loaded micelles, free DTX, and PBS. The drug was given on days 0, 3, 6, and 9 at a dosage of 10 mg DTX equiv/kg. Data are presented as mean ± SD ($n = 6$). (B) Body weight changes of nude mice following different treatments within 21 days. (C) Photographs of tumor blocks collected from different treatment groups on day 21. (D) Tumor weight of mice in different treatment groups on day 21; data are presented as mean ± SD ($n = 6$). $^*p < 0.05$, $^{**}p < 0.01$, $^{***}p < 0.001$. (E) H&E-stained liver and tumor sections, and TUNEL analysis of tumor tissues excised from subcutaneous U87MG glioma-bearing nude mice following 21 day treatment with DTX-loaded cRGD20/TAT10 CMs (I), cRGD20 CMs (II), PEG CMs (III), free DTX (IV), and PBS (V). The yellow arrows indicate hepatocellular necrosis. The images were obtained using a Leica microscope at 400× magnification. The scale bar is 50 μm.

size and stability in vivo. In time, the fluorescence of PEG CMs at the tumor gradually decreased probably because PEG CMs cannot be efficiently endocytosed by the tumor cells. Compared to PEG CMs, cRGD20 CMs displayed better tumor retention due to receptor-mediated endocytosis. Surprisingly, the cRGD20/TAT10 CM-treated mice possessed the most intensive fluorescence at the tumor site probably because efficient cellular uptake facilitated further accumulation of cRGD20/TAT10 CMs in tumor tissue. Another possible reason is that TAT peptide may help the micelles to penetrate deep into tumor tissues, resulting in better tumor retention. The ex vivo images (Figure 5C) also showed that the cRGD20/TAT10 CMs displayed the strongest tumor accumulation among the three groups and, importantly, showed weak uptake in normal organs, suggesting that TAT peptide was well shielded by the PEG layer in vivo, thus reducing nonspecific cell penetration.

Furthermore, the biodistribution of DTX using different formulations was investigated using U87MG tumor-bearing mice (Figure 5D). At 12 h after tail vein injection, the DTX levels in the main organs and the tumor were measured by HPLC. When DTX-loaded micelles were used, DTX was mainly located in the liver and tumor tissue. Compared to free DTX, DTX loaded in the micelles accumulated more strongly in tumor tissue due to the longer circulating time of the micelles. Notably, cRGD20/TAT10 CMs induced the highest tumor DTX level (8.6% ID/g), which could probably be attributed to efficient cellular uptake and deep tumor penetration.

3.6. Tumor Penetration. From the in vivo imaging, we speculated that TAT peptide may help micelles to penetrate the tumor tissue. Therefore, the distribution of micelles at the tumor periphery or in the tumor interior 12 h after tail vein injection of different Cy5-labeled micelles was observed by confocal microscopy. The blood vessels were stained with CD31, and cell nuclei were stained with DAPI. As shown in Figure 6A, PEG CMs were only located at the tumor periphery where abundant blood vessels are present, and little micelles were distributed in the depth of tumor, probably due to the extracellular barriers, such as high interstitial fluid pressure and reduced transcapillary pressure gradients.[1] Although the cRGD20 CMs presented a stronger fluorescence compared to the PEG CMs, limited tumor penetration was observed. Surprisingly, cRGD20/TAT10 CMs displayed bright fluorescence not only in the abundant blood vessels at the tumor edge but also in the avascular regions. Distribution of micelles in the tumor interior (Figure 6B) also revealed a similar trend that cRGD20/TAT10 CMs penetrated deeper into the tumor as compared to the other micelles. Notably, the enlarged pictures in Figure 6B clearly show the strongest cellular uptake of cRGD20/TAT10 CMs. The high tumor penetration of cRGD20/TAT20 CMs may probably be due to two aspects. First, it was reported that RGD peptide can also target $\alpha_v\beta_3$-overexpressing neovasculature in tumor tissue.[49] Therefore, selective and efficient penetration of neovasculature by cRGD20/TAT20 CMs may increase the number of micelles entering the tumor tissue. Second, the rapid uptake of cRGD20/TAT20 CMs in U87MG cells would create higher diffusion gradients, which enhance the transport rate of micelles into the tumor.[50,51] This possibly explains why cRGD20/TAT10 CMs exhibited the most efficient tumor penetration among the micelles tested. Some other studies, in which no reversibly cross-linked nanosystems were used, also demonstrated that the application of a combination of a targeting ligand and CPP could facilitate tumor penetration (liposomes,[52] PEG−PCL nanoparticles,[53] and mesoporous silica nanoparticles[54]).

3.7. In Vivo Antitumor Efficacy of cRGD20/TAT10 CMs. The in vivo antitumor efficacy of DTX-loaded cRGD20/TAT10 CMs was evaluated using a U87MG subcutaneous glioma model in nude mice. In comparison to DTX-loaded PEG CMs, DTX-loaded cRGD20 CMs exhibited a stronger tumor inhibition effect, probably due to receptor-mediated endocytosis (Figure 7A). Importantly, the tumor growth was nearly completely terminated by treatment with DTX-loaded cRGD20/TAT10 CMs. This superior antitumor efficacy was closely related to the high tumor accumulation and penetration, efficient cellular uptake, and subsequent rapid drug release as demonstrated above. Although free DTX also showed some tumor inhibition effect, significant mice body weight loss was found during therapy (Figure 7B), indicating its systemic toxicity to nude mice. However, the micelle-treated group did not show significant body weight decrease, implying good tolerance of nude mice to DTX-loaded micelles. Figure 7C,D shows the tumors excised from each treatment group and corresponding tumor weights, respectively, further confirming the superior antitumor efficacy of DTX-loaded cRGD20/TAT10 CMs. H&E staining (Figures 7E and S11) depicted the histological morphology of main organs and tumors in each group. It was noticed that serious damage was observed (yellow arrows) in liver tissue for the free DTX-treated group, indicating the hepatotoxicity of free DTX, whereas no obvious change was found in normal organs for the micelle-treated groups compared to the PBS-treated group. The tumors of the DTX-loaded cRGD20/TAT10 CM-treated group exhibited large areas of necrosis, and TUNEL staining further showed large amounts of apoptotic cells (brown dots), with a significantly higher IOD value of TUNEL-positive cells than for other groups (Figure S12), demonstrating that DTX-loaded cRGD20/TAT10 CMs had a superior antitumor effect.

4. CONCLUSIONS

In this study, dual-ligand-functionalized reversibly cross-linked micelles were simply engineered by using PEG-P(DTC-*co*-CL) block copolymers with different PEG lengths (2, 5, and 6k), of which TAT was attached to PEG_{2k} and cRGD to PEG_{6k}. In vitro studies showed that cRGD20/TAT10 CMs markedly increased the cellular uptake compared to cRGD20 CMs or PEG CMs and exhibited the strongest cytotoxicity against U87MG cells after loading with DTX. Mechanistic studies revealed that the cellular uptake of cRGD20/TAT10 CMs was receptor- and energy-dependent and mainly took place via caveolae-mediated endocytosis combined with efficient escape from lysosomes. Importantly, cRGD20/TAT10 CMs remained stable in the circulation in vivo due to shielding of TAT and cross-linking of micelles. cRGD20/TAT10 CMs also showed a high accumulation and deep tumor penetration in U87MG subcutaneous glioma, leading to almost complete inhibition of tumor growth. Therefore, combining the dual-ligand strategy with reversibly cross-linked micelles may provide an effective way to realize high tumor penetration and inhibition.

■ ASSOCIATED CONTENT

Ⓢ Supporting Information

The Supporting Information is available free of charge on the ACS Publications website at DOI: 10.1021/acsami.7b12439.

> Materials, synthesis of polymers, characterization, serum stability and GSH-triggered de-cross-linking of micelles, reduction-triggered drug release of DTX-loaded micelles, MTT assay, and cellular uptake of micelles; synthetic routes of cRGD-PEG_{6k}-P(DTC-CL) and TAT-PEG_{2k}-P(DTC-CL); ^{1}H NMR spectra for $mPEG_{5k}$-P(DTC-*co*-CL), MAL-PEG_{6k}-P(DTC-*co*-CL), cRGD-PEG_{6k}-P-(DTC-*co*-CL), MAL-PEG_{2k}-P(DTC-*co*-CL), and TAT-PEG_{2k}-P(DTC-*co*-CL); size distribution and ζ potential of blank micelles; characterization of DTX-loaded micelles; UV spectra of cRGD20/TAT10 CMs; cytotoxicity of blank micelles and endocytic inhibitors; and histological analysis of main organs after therapy (PDF)

■ AUTHOR INFORMATION

Corresponding Authors

*E-mail: j.feijen@utwente.nl (J.F.).
*E-mail: zyzhong@suda.edu.cn. Tel/Fax: +86-512-65880098 (Z.Z.).

ORCID

Fenghua Meng: 0000-0002-8608-7738
Chao Deng: 0000-0001-7697-9874
Jan Feijen: 0000-0003-1202-4328
Zhiyuan Zhong: 0000-0003-4175-4741

Notes

The authors declare no competing financial interest.

■ ACKNOWLEDGMENTS

This work was financially supported by the National Natural Science Foundation of China (NSFC 51473111, 51561135010, and 51633005).

■ REFERENCES

(1) Jain, R. K.; Stylianopoulos, T. Delivering Nanomedicine to Solid Tumors. *Nat. Rev. Clin. Oncol.* **2010**, 7, 653−664.

(2) Deng, C.; Jiang, Y.; Cheng, R.; Meng, F.; Zhong, Z. Biodegradable Polymeric Micelles for Targeted and Controlled Anticancer Drug Delivery: Promises, Progress and Prospects. *Nano Today* **2012**, *7*, 467−480.

(3) Barua, S.; Mitragotri, S. Challenges Associated with Penetration of Nanoparticles across Cell and Tissue Barriers: A Review of Current Status and Future Prospects. *Nano Today* **2014**, *9*, 223−243.

(4) Blanco, E.; Shen, H.; Ferrari, M. Principles of Nanoparticle Design for Overcoming Biological Barriers to Drug Delivery. *Nat. Biotechnol.* **2015**, *33*, 941−951.

(5) Vasir, J. K.; Labhasetwar, V. Biodegradable Nanoparticles for Cytosolic Delivery of Therapeutics. *Adv. Drug Delivery Rev.* **2007**, *59*, 718−728.

(6) Chou, L. Y.; Ming, K.; Chan, W. C. Strategies for the Intracellular Delivery of Nanoparticles. *Chem. Soc. Rev.* **2011**, *40*, 233−245.

(7) Miura, Y.; Takenaka, T.; Toh, K.; Wu, S.; Nishihara, H.; Kano, M. R.; Ino, Y.; Nomoto, T.; Matsumoto, Y.; Koyama, H.; Cabral, H.; Nishiyama, N.; Kataoka, K. Cyclic RGD-Linked Polymeric Micelles for Targeted Delivery of Platinum Anticancer Drugs to Glioblastoma through the Blood−Brain Tumor Barrier. *ACS Nano* **2013**, *7*, 8583−8592.

(8) Zhu, Y.; Zhang, J.; Meng, F.; Deng, C.; Cheng, R.; Feijen, J.; Zhong, Z. cRGD-Functionalized Reduction-Sensitive Shell-Sheddable Biodegradable Micelles Mediate Enhanced Doxorubicin Delivery to Human Glioma Xenografts in Vivo. *J. Controlled Release* **2016**, *233*, 29−38.

(9) Yue, J.; Liu, S.; Wang, R.; Hu, X.; Xie, Z.; Huang, Y.; Jing, X. Transferrin-Conjugated Micelles: Enhanced Accumulation and Antitumor Effect for Transferrin-Receptor-Overexpressing Cancer Models. *Mol. Pharmaceutics* **2012**, *9*, 1919−1931.

(10) Kim, D.; Lee, E. S.; Oh, K. T.; Gao, Z. G.; Bae, Y. H. Doxorubicin-Loaded Polymeric Micelle Overcomes Multidrug Resistance of Cancer by Double-Targeting Folate Receptor and Early Endosomal pH. *Small* **2008**, *4*, 2043−2050.

(11) Hoang, B.; Ekdawi, S. N.; Reilly, R. M.; Allen, C. Active Targeting of Block Copolymer Micelles with Trastuzumab Fab Fragments and Nuclear Localization Signal Leads to Increased Tumor Uptake and Nuclear Localization in Her2-Overexpressing Xenografts. *Mol. Pharmaceutics* **2013**, *10*, 4229−4241.

(12) Wang, F.; Wang, Y.; Zhang, X.; Zhang, W.; Guo, S.; Jin, F. Recent Progress of Cell-Penetrating Peptides as New Carriers for Intracellular Cargo Delivery. *J. Controlled Release* **2014**, *174*, 126−136.

(13) Vandenbroucke, R. E.; De Smedt, S. C.; Demeester, J.; Sanders, N. N. Cellular Entry Pathway and Gene Transfer Capacity of Tat-Modified Lipoplexes. *Biochim. Biophys. Acta, Biomembr.* **2007**, *1768*, 571−579.

(14) Xiong, X. B.; Uludag, H.; Lavasanifar, A. Virus-Mimetic Polymeric Micelles for Targeted Sirna Delivery. *Biomaterials* **2010**, *31*, 5886−5893.

(15) Pan, L.; Liu, J.; He, Q.; Wang, L.; Shi, J. Overcoming Multidrug Resistance of Cancer Cells by Direct Intranuclear Drug Delivery Using Tat-Conjugated Mesoporous Silica Nanoparticles. *Biomaterials* **2013**, *34*, 2719−2730.

(16) Torchilin, V. P. Tat Peptide-Mediated Intracellular Delivery of Pharmaceutical Nanocarriers. *Adv. Drug Delivery Rev.* **2008**, *60*, 548−558.

(17) Huang, Y.; Jiang, Y.; Wang, H.; Wang, J.; Shin, M. C.; Byun, Y.; He, H.; Liang, Y.; Yang, V. C. Curb Challenges of the "Trojan Horse" Approach: Smart Strategies in Achieving Effective yet Safe Cell-Penetrating Peptide-Based Drug Delivery. *Adv. Drug Delivery Rev.* **2013**, *65*, 1299−1315.

(18) Gump, J. M.; Dowdy, S. F. Tat Transduction: The Molecular Mechanism and Therapeutic Prospects. *Trends Mol. Med.* **2007**, *13*, 443−448.

(19) Zhu, L.; Kate, P.; Torchilin, V. P. Matrix Metalloprotease 2-Responsive Multifunctional Liposomal Nanocarrier for Enhanced Tumor Targeting. *ACS Nano* **2012**, *6*, 3491−3498.

(20) Kuai, R.; Yuan, W.; Qin, Y.; Chen, H.; Tang, J.; Yuan, M.; Zhang, Z.; He, Q. Efficient Delivery of Payload into Tumor Cells in a Controlled Manner by Tat and Thiolytic Cleavable PEG Co-Modified Liposomes. *Mol. Pharmaceutics* **2010**, *7*, 1816−1826.

(21) Koren, E.; Apte, A.; Jani, A.; Torchilin, V. P. Multifunctional PEGylated 2C5-Immunoliposomes Containing pH-Sensitive Bonds and Tat Peptide for Enhanced Tumor Cell Internalization and Cytotoxicity. *J. Controlled Release* **2012**, *160*, 264−273.

(22) Sethuraman, V. A.; Bae, Y. H. Tat Peptide-Based Micelle System for Potential Active Targeting of Anti-Cancer Agents to Acidic Solid Tumors. *J. Controlled Release* **2007**, *118*, 216−224.

(23) Estrella, V.; Chen, T.; Lloyd, M.; Wojtkowiak, J.; Cornnell, H. H.; Ibrahim-Hashim, A.; Bailey, K.; Balagurunathan, Y.; Rothberg, J. M.; Sloane, B. F.; Johnson, J.; Gatenby, R. A.; Gillies, R. J. Acidity Generated by the Tumor Microenvironment Drives Local Invasion. *Cancer Res.* **2013**, *73*, 1524−1535.

(24) Trédan, O.; Galmarini, C. M.; Patel, K.; Tannock, I. F. Drug Resistance and the Solid Tumor Microenvironment. *J. Natl. Cancer Inst.* **2007**, *99*, 1441−1454.

(25) Kessenbrock, K.; Plaks, V.; Werb, Z. Matrix Metalloproteinases: Regulators of the Tumor Microenvironment. *Cell* **2010**, *141*, 52−67.

(26) Fang, Y.; Jiang, Y.; Zou, Y.; Meng, F.; Zhang, J.; Deng, C.; Sun, H.; Zhong, Z. Targeted Glioma Chemotherapy by Cyclic RGD Peptide-Functionalized Reversibly Core-Crosslinked Multifunctional Poly(Ethylene Glycol)-*b*-Poly(*ε*-Caprolactone) Micelles. *Acta Biomater.* **2017**, *50*, 396−406.

(27) Jia, T.; Sun, Z.; Lu, Y.; Gao, J.; Zou, H.; Xie, F.; Zhang, G.; Xu, H.; Sun, D.; Yu, Y.; Zhong, Y. A Dual Brain-Targeting Curcumin-Loaded Polymersomes Ameliorated Cognitive Dysfunction in Intrahippocampal Amyloid-*β*1-42-Injected Mice. *Int. J. Nanomed.* **2016**, *11*, 3765−3775.

(28) Talelli, M.; Barz, M.; Rijcken, C. J.; Kiessling, F.; Hennink, W. E.; Lammers, T. Core-Crosslinked Polymeric Micelles: Principles, Preparation, Biomedical Applications and Clinical Translation. *Nano Today* **2015**, *10*, 93−117.

(29) Zou, Y.; Fang, Y.; Meng, H.; Meng, F.; Deng, C.; Zhang, J.; Zhong, Z. Self-Crosslinkable and Intracellularly Decrosslinkable Biodegradable Micellar Nanoparticles: A Robust, Simple and Multifunctional Nanoplatform for High-Efficiency Targeted Cancer Chemotherapy. *J. Controlled Release* **2016**, *244*, 326−335.

(30) Luo, Y.; Yang, J.; Yan, Y.; Li, J.; Shen, M.; Zhang, G.; Mignani, S.; Shi, X. RGD-Functionalized Ultrasmall Iron Oxide Nanoparticles for Targeted T(1)-Weighted MR Imaging of Gliomas. *Nanoscale* **2015**, *7*, 14538−14546.

(31) Zhu, Y.; Wang, X.; Chen, J.; Zhang, J.; Meng, F.; Deng, C.; Cheng, R.; Feijen, J.; Zhong, Z. Bioresponsive and Fluorescent Hyaluronic Acid-Iodixanol Nanogels for Targeted X-Ray Computed Tomography Imaging and Chemotherapy of Breast Tumors. *J. Controlled Release* **2016**, *244*, 229−239.

(32) Zhu, Y.; Cheng, L.; Cheng, L.; Huang, F.; Hu, Q.; Li, L.; Tian, C.; Wei, L.; Chen, D. Folate and Tat Peptide Co-Modified Liposomes Exhibit Receptor-Dependent Highly Efficient Intracellular Transport of Payload in Vitro and in Vivo. *Pharm. Res.* **2014**, *31*, 3289−3303.

(33) Cardozo, A. K.; Buchillier, V.; Mathieu, M.; Chen, J.; Ortis, F.; Ladriere, L.; Allaman-Pillet, N.; Poirot, O.; Kellenberger, S.; Beckmann, J. S.; Eizirik, D. L.; Bonny, C.; Maurer, F. Cell-Permeable Peptides Induce Dose- and Length-Dependent Cytotoxic Effects. *Biochim. Biophys. Acta, Biomembr.* **2007**, *1768*, 2222−2234.

(34) Li, C.; Zhou, Y.; Peng, X.; Du, L.; Tian, H.; Yang, G.; Niu, J.; Wu, W. Sulforaphane Inhibits Invasion Via Activating ERK1/2 Signaling in Human Glioblastoma U87MG and U373MG Cells. *PLoS One* **2014**, *9*, No. e90520.

(35) Yamano, S.; Dai, J.; Yuvienco, C.; Khapli, S.; Moursi, A. M.; Montclare, J. K. Modified Tat Peptide with Cationic Lipids Enhances Gene Transfection Efficiency Via Temperature-Dependent and Caveolae-Mediated Endocytosis. *J. Controlled Release* **2011**, *152*, 278−285.

(36) Lee, E. S.; Gao, Z.; Kim, D.; Park, K.; Kwon, I. C.; Bae, Y. H. Super pH-Sensitive Multifunctional Polymeric Micelle for Tumor pH(e) Specific Tat Exposure and Multidrug Resistance. *J. Controlled Release* **2008**, *129*, 228−236.

(37) Monti, D. M.; Guarnieri, D.; Napolitano, G.; Piccoli, R.; Netti, P.; Fusco, S.; Arciello, A. Biocompatibility, Uptake and Endocytosis Pathways of Polystyrene Nanoparticles in Primary Human Renal Epithelial Cells. *J. Biotechnol.* **2015**, *193*, 3−10.

(38) Belting, M. Heparan Sulfate Proteoglycan as a Plasma Membrane Carrier. *Trends Biochem. Sci.* **2003**, *28*, 145−151.

(39) Pan, R.; Xu, W.; Ding, Y.; Lu, S.; Chen, P. Uptake Mechanism and Direct Translocation of a New CPP for siRNA Delivery. *Mol. Pharmaceutics* **2016**, *13*, 1366−1374.

(40) Sahay, G.; Alakhova, D. Y.; Kabanov, A. V. Endocytosis of Nanomedicines. *J. Controlled Release* **2010**, *145*, 182−195.

(41) Joo, K.-I.; Lei, Y.; Lee, C.-L.; Lo, J.; Hamm-Alvarez, S. F.; Wang, P.; et al. Site-Specific Labeling of Enveloped Viruses with Quantum Dots for Single Virus Tracking. *ACS Nano* **2008**, *2*, 1553−1562.

(42) Iversen, T.-G.; Skotland, T.; Sandvig, K. Endocytosis and Intracellular Transport of Nanoparticles: Present Knowledge and Need for Future Studies. *Nano Today* **2011**, *6*, 176−185.

(43) Cao, J.; Xie, X.; Lu, A.; He, B.; Chen, Y.; Gu, Z.; Luo, X. Cellular Internalization of Doxorubicin Loaded Star-Shaped Micelles with Hydrophilic Zwitterionic Sulfobetaine Segments. *Biomaterials* **2014**, *35*, 4517−4524.

(44) Peng, S. F.; Tseng, M. T.; Ho, Y. C.; Wei, M. C.; Liao, Z. X.; Sung, H. W. Mechanisms of Cellular Uptake and Intracellular Trafficking with Chitosan/DNA/Poly (γ-Glutamic Acid) Complexes as a Gene Delivery Vector. *Biomaterials* **2011**, *32*, 239−248.

(45) Meng, F.; Hennink, W. E.; Zhong, Z. Reduction-Sensitive Polymers and Bioconjugates for Biomedical Applications. *Biomaterials* **2009**, *30*, 2180−2198.

(46) Shi, Y.; Lammers, T.; Storm, G.; Hennink, W. E. Physico-Chemical Strategies to Enhance Stability and Drug Retention of Polymeric Micelles for Tumor-Targeted Drug Delivery. *Macromol. Biosci.* **2017**, *17*, No. 1600160.

(47) Kim, H.; Lee, Y.; Lee, I. H.; Kim, S.; Kim, D.; Saw, P. E.; Lee, J.; Choi, M.; Kim, Y. C.; Jon, S. Synthesis and Therapeutic Evaluation of an Aptide-Docetaxel Conjugate Targeting Tumor-Associated Fibronectin. *J. Controlled Release* **2014**, *178*, 118−124.

(48) Jain, S.; Bhankur, N.; Swarnakar, N. K.; Thanki, K. Phytantriol Based "Stealth" Lyotropic Liquid Crystalline Nanoparticles for Improved Antitumor Efficacy and Reduced Toxicity of Docetaxel. *Pharm. Res.* **2015**, *32*, 3282−3292.

(49) Zhu, S.; Qian, L.; Hong, M.; Zhang, L.; Pei, Y.; Jiang, Y. RGD-Modified PEG-PAMAM-Dox Conjugate: In Vitro and in Vivo Targeting to Both Tumor Neovascular Endothelial Cells and Tumor Cells. *Adv. Mater.* **2011**, *23*, H84−H89.

(50) Wang, M.; Thanou, M. Targeting Nanoparticles to Cancer. *Pharmacol. Res.* **2010**, *62*, 90−99.

(51) Gao, Z.; Zhang, L.; Sun, Y. Nanotechnology Applied to Overcome Tumor Drug Resistance. *J. Controlled Release* **2012**, *162*, 45−55.

(52) Zong, T.; Mei, L.; Gao, H.; Cai, W.; Zhu, P.; Shi, K.; Chen, J.; Wang, Y.; Gao, F.; He, Q. Synergistic Dual-Ligand Doxorubicin Liposomes Improve Targeting and Therapeutic Efficacy of Brain Glioma in Animals. *Mol. Pharmaceutics* **2014**, *11*, 2346−2357.

(53) Gao, H.; Zhang, S.; Cao, S.; Yang, Z.; Pang, Z.; Jiang, X. Angiopep-2 and Activatable Cell-Penetrating Peptide Dual-Functionalized Nanoparticles for Systemic Glioma-Targeting Delivery. *Mol. Pharmaceutics* **2014**, *11*, 2755−2763.

(54) Pan, L.; Liu, J.; He, Q.; Shi, J. MSN-Mediated Sequential Vascular-to-Cell Nuclear-Targeted Drug Delivery for Efficient Tumor Regression. *Adv. Mater.* **2014**, *26*, 6742−6748.

DOI: 10.1021/acsami.7b12439
ACS Appl. Mater. Interfaces 2017, 9, 35651−35663